Unsteady development of a deformable bubble rising in a quiescent liquid

Alpana Agarwal, C.F. Tai, J.N. Chung [*]

Department of Mechanical and Aerospace Engineering, University of Florida, Gainesville, FL 32611, USA

ARTICLE INFO

ABSTRACT

An accurate finite-volume based numerical method for the simulation of an isothermal two-phase flow, consisting of a rising deformable bubble translating in a quiescent, unbounded liquid, is presented. This direct simulation method is built on a sharp interface concept and developed on an Eulerian, Cartesian fixed-grid with a cut-cell scheme and marker points to track the moving interface. The unsteady Navier–Stokes equations in both liquid and gas phases are solved separately. The mass continuity and momentum flux conditions are explicitly matched at the true surface phase boundary to determine the evolving interface shape and movement of the bubble. The highlights of this method are that it utilizes a combined Eulerian–Lagrangian approach, and is capable of treating the interface as a sharp discontinuity. A fixed underlying grid is used to represent the control volume. The interface, however, is denoted by a separate set of marker particles which move along with the interface. A quadratic curve fitting algorithm with marker points is used to yield smooth and accurate information of the interface curvatures. This numerical scheme can handle a wide range of density and viscosity ratios. The bubble is assumed to be spherical and at rest initially, but deforms as it rises through the liquid pool due to buoyancy. Additionally, the flow is assumed to be axisymmetric and incompressible. The bubble deformation and dynamic motion are characterized by the Reynolds number, the Weber number, the density ratio and the viscosity ratio. The effects of these parameters on the translational bubble dynamics and shape are given and the physical mechanisms are explained and discussed. Results for the shape, velocity profile and various forces acting on the bubble are presented here as a function of time until the bubble reaches terminal velocity. The range of Reynolds numbers investigated is $1 < Re < 100$, and that of Weber number is $1 < We < 10$.

1. Introduction

Multiphase flows are encountered in a variety of engineering applications, including the power, chemical, petroleum and electronics industries among others. Until about twenty years ago, these problems were considered too complicated to be solved in entirety, and only analytical solutions for limiting cases [1] were attempted. However, due to an exponential increase in computing power in the recent years, they can now be solved by direct numerical simulation.

In the early development of computational multiphase flows, some researchers adopted the curvilinear grid system [2–5]. This approach is simple in theory but poses practical difficulties. In order to describe the deformation of the interface between different phases, powerful grid generation is required. The grid has to be updated frequently to obtain a convergent solution, making it very computationally intensive. In recent multiphase computations, several Cartesian grid methods have been introduced: the sharp interface method (SIM) [6,7], the immersed boundary method

(IBM) [8,9], the volume-of-fluid (VOF) method [10,11], the level-set method [12,13], the hybrid level-set and volume-of-fluid method [14,15], the phase-field method [16] etc. Based on the computational framework, SIM and IBM are classified as mixed Eulerian–Lagrangian while the level-set, VOF and phase-field methods are in the Eulerian category [17].

In this research, the sharp interface method (SIM) which is a branch of the mixed Eulerian–Lagrangian Cartesian grid methods is employed to simulate complex geometries. In SIM, a Cartesian grid forms the background mesh and explicit interfaces are used to describe the shapes of the objects on this background grid. The interface is explicit and is constructed by a sequence of marker points. With these marker points, the shape and location of the interface are determined by designated interpolation procedures, while the overall fluid flow is computed based on the fixed Cartesian grid. The interfacial dynamics associated with the moving/fixed boundaries is satisfied simultaneously with the bulk fluid flow. The advantage provided by SIM is that it exactly follows the continuum model for fluids. The interface has zero thickness, and there is no approximation involved in either the kinematic or the dynamic model. The primary variables at the interface are computed via the interfacial conditions.

[*] Corresponding author.
E-mail address: jnchung@ufl.edu (J.N. Chung).

In SIM, one needs to define the relationship between the background grid and the explicit interface. Because the interface does not conform to the grid, the cells containing the interface will be cut and form non-rectangular cut-cells. These cut-cells need to be treated differently from ordinary rectangular cells. In this research, a cut-cell procedure based on [7,18,19] is employed to treat the cells near the interface. In the cut-cell approach, each segment of the cut-cell is merged into a neighboring cell or assigned the identity of the original Cartesian cell. Hence, even though the underlying grid is Cartesian, the cut-cells are reconstructed to become the non-rectangular cells and the cut-sides will form the interface. After the reconstruction, the entire grid is filled with the rectangular grid and non-rectangular grid. The shapes of the cut-cells so formed can be triangular, trapezoidal or pentagonal. SIM with the cut-cell approach (SIMCC) can handle the sharp discontinuity in fluid properties resulting from the presence of the interface. Therefore SIMCC can achieve greater accuracy [7,19]. Among the Eulerian–Lagrangian approaches, SIMCC gives the best accuracy, especially near a solid boundary. Fig. 1 is an example of the type of grid system used in SIMCC. An explicit interface constructed by marker points will divide the entire domain into different phases. The grid has two types of cells, rectangular cells away from the interface and cut-cells in its vicinity. The cut-cell approach also ensures that the total number of cells does not change during the computation.

The present research features an improvement in the interfacial advection technique, which enables SIMCC to handle the tangential stress balance at the interface. This extends the range and capability of SIMCC to lower Reynolds numbers. This had not been possible earlier, and it is shown conclusively in this research that the contribution from viscous tangential stress at the interface is quite substantial for $Re \leqslant O(1)$ and can not be ignored.

In summary, the new contribution of the current manuscript is on the unsteady hydrodynamics of a bubble. As far as we know, this paper is the first to present time-dependent drag of a deformable bubble.

2. Problem statement

2.1. Problem description

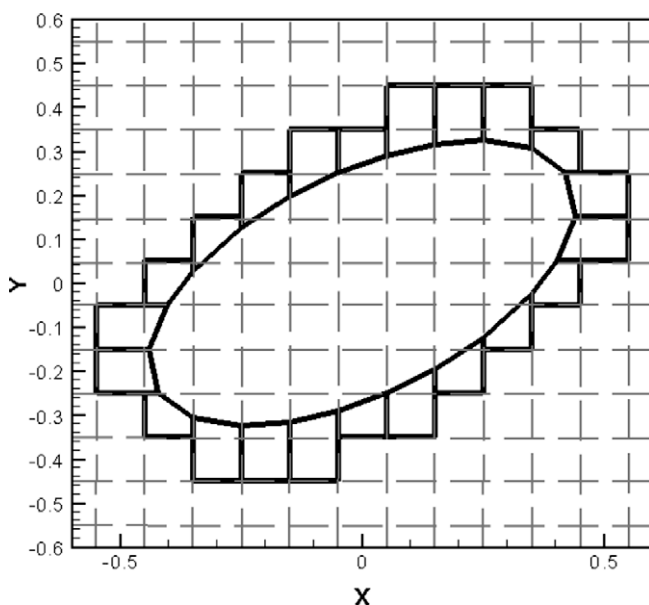The problem consists of an isolated vapor/gas bubble moving in a quiescent, unbounded liquid pool due to buoyancy. The there is no heat or mass transfer between the two phases. The bubble is free to deform under the action of viscous forces, surface tension etc. In reality, this situation can occur when a bubble is generated in a vessel with dimensions large as compared to the size of the bubble.

2.2. Assumptions

There are several simplifying assumptions that have been made to model this problem. These are:

1. Both phases are Newtonian fluids.
2. Incompressible flow for liquid and gas phases.
3. Constant fluid properties for liquid and gas phase.
4. No heat and mass transfer at the bubble interface.
5. The temperature remains constant throughout.
6. The entire flow is axisymmetric.
7. The hydrostatic pressure and the dynamic pressure can be decoupled and solved for separately.

The assumption of axisymmetry allows us to use 2d Navier–Stokes equation in cylindrical coordinates. The hydrostatic pressure is computed as a function of the distance from the free surface. The dynamic pressure is computed during the main flow simulation. This can be done because the density is constant for each phase, and is a common practice in simulations of bubble dynamics [20].

2.3. Governing equations

The sharp interface method with cut-cell scheme (SIMCC) is adopted to treat the moving interface. In the SIM, the interface is a true phase boundary with zero thickness and the governing equations of each phase are distinct. The transport fluxes are matched between the two phases at the interface. If there are N phases in the computational domain, there will be N sets of governing equations. In isothermal two-phase flow, mass and momentum conservation equations for the liquid and gas phase are developed separately.

Based on the assumptions mentioned and the coordinates system and schematic given in Fig. 2, the dimensional governing equations are listed:

2.3.1. Liquid phase

$$\vec{\nabla} \cdot \vec{u}_l = 0, \tag{1a}$$

$$\rho_l \left[\frac{\partial \vec{u}_l}{\partial t} + \vec{\nabla} \cdot (\vec{u}_l \vec{u}_l) \right] = -\vec{\nabla} p_l + \rho_l \vec{g} + \mu_l \nabla^2 \vec{u}_l. \tag{1b}$$
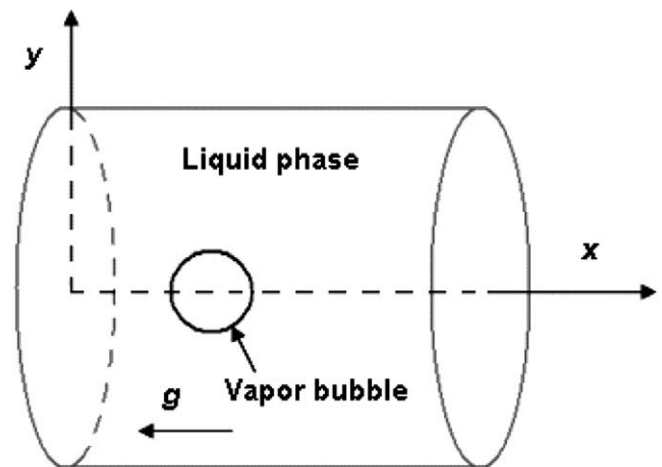

Fig. 1. Example of mixed structured and unstructured grid.

Fig. 2. Cylindrical coordinate system.

2.3.2. Vapor phase

$$\vec{\nabla} \cdot \vec{u}_v = 0, \tag{2a}$$

$$\rho_v \left[\frac{\partial \vec{u}_v}{\partial t} + \vec{\nabla} \cdot (\vec{u}_v \vec{u}_v) \right] = -\vec{\nabla} p_v + \rho_v \vec{g} + \mu_v \nabla^2 \vec{u}_v, \tag{2b}$$

where subscripts 'l' and 'v' denote the liquid and vapor phase, respectively; $\vec{u}$ is the velocity vector, p is the dynamic pressure, ρ is the density and μ is the dynamic viscosity. The force balance and velocity continuity at the interface should be satisfied.

2.3.3. Interfacial conditions

$$\vec{u}_v = \vec{u}_l = \vec{u}_{int}, \tag{3a}$$

$$P_l - P_v + \sigma\kappa = \vec{n} \cdot \left(\bar{\bar{\tau}}_l \cdot \vec{n} \right) - \vec{n} \cdot \left(\bar{\bar{\tau}}_v \cdot \vec{n} \right), \tag{3b}$$

$$\vec{s} \cdot \left(\bar{\bar{\tau}}_l \cdot \vec{n} \right) = \vec{s} \cdot \left(\bar{\bar{\tau}}_v \cdot \vec{n} \right), \tag{3c}$$

where $\bar{\bar{\tau}}$ represents the viscous stress tensor; P is the total pressure, σ is the surface tension coefficient; $\vec{n}$ is the normal vector and $\vec{s}$ is the tangential vector; κ is the curvature of the interface and the subscript int denotes the interface.

2.4. Non-dimensionalization

In this work, all the computational quantities are non-dimensional. The Navier–Stokes equation for each phase as well as the interfacial conditions must be non-dimensionalized first. The reference scales are the initial diameter d of the bubble, its terminal velocity U and the characteristic time is d/U. With these reference scales, the dimensionless variables are defined as:

$$\vec{x}^* = \vec{x}/d, \quad \vec{u}^* = \vec{u}/U, \quad t^* = tU/d, \quad p^* = p/(\rho_{ref} U^2),$$

$$\rho^* = (\rho/\rho_{ref}), \quad \mu^* = (\mu/\mu_{ref}).$$

Here properties of the liquid phase are used as reference. After the non-dimensionalization procedure, the governing equations and the interfacial conditions can be written as follows (for convenience the asterisks for dimensionless quantities are dropped from this point on):

2.4.1. Liquid phase

$$\vec{\nabla} \cdot \vec{u}_l = 0, \tag{4a}$$

$$\frac{\partial \vec{u}_l}{\partial t} + \vec{\nabla} \cdot (\vec{u}_l \vec{u}_l) = -\vec{\nabla} p_l + \frac{1}{Re} \nabla^2 \vec{u}_l. \tag{4b}$$

2.4.2. Vapor phase

$$\vec{\nabla} \cdot \vec{u}_v = 0, \tag{5a}$$

$$\frac{\partial}{\partial t} \left(\frac{\rho_v}{\rho_l} \vec{u}_v \right) + \vec{\nabla} \cdot \left(\frac{\rho_v}{\rho_l} \vec{u}_v \vec{u}_v \right) = -\vec{\nabla} p_v + \frac{1}{Re} \vec{\nabla} \cdot \left(\frac{\rho_v}{\rho_l} \vec{\nabla} \vec{u}_v \right), \tag{5b}$$

where the dimensionless parameter Re is the Reynolds number, defined as

$$Re = \frac{\rho_l U d}{\mu_l}. \tag{6}$$

In the present study, $\frac{\rho_v}{\rho_l} = \frac{1}{1605}$ and $\frac{\mu_v}{\mu_l} = \frac{1}{22}$ which corresponds to water and air at room temperature.

2.4.3. Interfacial conditions

$$\vec{u}_v = \vec{u}_l = \vec{u}_{int}, \tag{7a}$$

$$P_l - P_v + \frac{\kappa}{We} = \frac{2}{Re} \left[\left(\frac{\partial u_n}{\partial n} \right)_l - \left(\frac{\mu_v}{\mu_l} \right) \left(\frac{\partial u_n}{\partial n} \right)_v \right], \tag{7b}$$

$$\left(\frac{\partial u_s}{\partial n} + \frac{\partial u_n}{\partial s} \right)_l = \left(\frac{\mu_v}{\mu_l} \right) \left(\frac{\partial u_s}{\partial n} + \frac{\partial u_n}{\partial s} \right)_v, \tag{7c}$$

where We is the Weber number defined as

$$We = \frac{\rho_l U^2 d}{\sigma}. \tag{8}$$

2.5. Geometry, computational domain and initial conditions

Since, this is an axisymmetric computation, a rectangular domain with a length of $58d$ and a width of $38d$ is used to simulate an unbounded liquid pool. This size of the domain was found to satisfy the far-field boundary conditions which require all the gradients to go to zero. A graded mesh has been used in both x- and y-directions, with the mesh becoming progressively refined near the section where the bubble motion and wake formation occurs. The gird is 300×100, with a grid spacing of 0.04 near the bubble. The simulation is started with an initially stationary liquid pool and a stationary spherical gas bubble of radius 0.5. Gravity acts in the negative x-direction, therefore the motion of the gas bubble occurs in the positive x-direction due to buoyancy forces.

2.6. Boundary conditions

The lower boundary is a plane of symmetry for the axisymmetric domain. Hence the symmetry boundary conditions apply. In keeping with the assumption of an unbounded liquid pool, a large domain of computation has been chosen. Therefore, it is reasonable to assume that the velocity gradient in the normal direction would be zero at the left, top and right boundaries. Hence, the far-field boundary condition is specified on the left, top and right wall.

3. Numerical method for modeling multiphase flows

In this section, the numerical method adopted for direct simulation of bubble is presented. As explained, a combined Eulerian–Lagrangian framework with the concept of an explicit sharp interface separating the two phases, is central to our approach. In other words, the interface is a true surface without any volume association. The interface is advanced using the normal stress balance. The key elements of the numerical technique are listed below. For more details refer to [21].
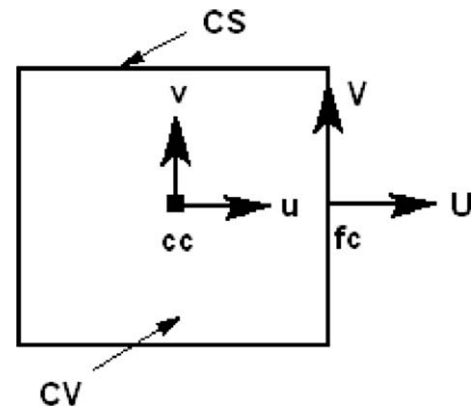

Fig. 3. Unit cell for non-staggered grid system.

3.1. Fractional step method within the finite-volume framework

In order to best enforce the conservation laws and to treat the discontinuity at the interface, the finite-volume method is used to discretize the governing equations. Within this framework, the governing equations listed before will be integrated over a finite control volume. This is called a unit cell as shown in Fig. 3. The integral forms of governing equations are given:

3.1.1. Continuity equation

$$\int_{cv} (\vec{u} \cdot \vec{n}) \, dV = 0. \tag{9}$$

3.1.2. Momentum equation

$$\int_{cv} \frac{\partial \vec{u}}{\partial t} \, dV + \int_{cs} \vec{u}(\vec{u} \cdot \vec{n}) \, dS = -\int_{cs} p\vec{n} \, dS + \frac{1}{Re} \int_{cs} \vec{\nabla} \vec{u} \cdot \vec{n} \, dS, \tag{10}$$

where cv and cs represent the control volume and the surface of the control volume, respectively. $\vec{n}$ is the outward normal vector from the control volume surface, $\vec{u}$ is the velocity vector and p is the pressure.

A cell-centered collocated (non-staggered) approach [22] on the Cartesian grid system is adopted, the primitive variables (velocity, pressure and temperature) are defined at the cell centers and the primary variables needed at the cell faces are evaluated by interpolation from respective variables at cell centers as shown in Fig. 3.

The fractional step method is a branch of pressure based predictor–corrector methods. The predict–correct procedure is not determined uniquely and can be constructed by different combinations of prediction and correction steps. The key point is that the governing equations can not be modified during the prediction procedure and the continuity equation must be included in last correction procedure since the continuity equation is not solved separately. Here, a second-order accurate two-step fractional step method [23–25] is used for advancing the solutions of the integral unsteady governing equations in time. In this approach, the solution is advanced from time step n to $n + 1$ through an intermediate diffusion–convection step. In the intermediate step, the momentum equations without the pressure gradient terms are first solved and advanced. The intermediate diffusion–convection momentum equation can be discretized as:

$$\int_{cv} \frac{\vec{u}^* - \vec{u}^n}{\Delta t} \, dV = -\frac{1}{2} \int_{cs} \left[3\vec{u}^n \left(\vec{U}^n \cdot \vec{n} \right) - \vec{u}^{n-1} \left(\vec{U}^{n-1} \cdot \vec{n} \right) \right] dS$$
$$+ \frac{1}{2Re} \int_{cs} \left(\vec{\nabla} \vec{u}^* + \vec{\nabla} \vec{u}^n \right) \cdot \vec{n} \, dS, \tag{11}$$

where $\vec{u}^*$ is the intermediate velocity at the cell center and $\vec{U}$ is the velocity at center of the cell face. The cell surface velocity is used to evaluate the fluxes in or out of a control volume. After $\vec{u}^*$ is determined, $\vec{U}^*$, the intermediate velocity at the center of cell face, is calculated by interpolating between the respective cell center velocities. The first term on the right hand side is the convective term. A second order accurate Adams–Bashforth scheme is used to discretize the convective term. The second term is the diffusive term that is discretized by the implicit Crank–Nicolson scheme. This eliminates the potential viscous instability that could be quite severe in the simulation of viscous flows. Once the intermediate velocity is obtained, the pressure is obtained by the correction step:

$$\int_{cv} \frac{\vec{u}^{n+1} - \vec{u}^*}{\Delta t} \, dV = -\int_{cv} \vec{\nabla} p^{n+1} \, dV. \tag{12}$$

In this pressure correction step, the final velocity $\vec{u}^{n+1}$ must satisfy the integral mass conservative equation, which can be written in the following form:

$$\int_{cs} \left(\vec{U}^{n+1} \cdot \vec{n} \right) dS = 0. \tag{13}$$

Therefore, the integral pressure correction equation can be expressed as:

$$-\int_{cs} \left(\vec{\nabla} p^{n+1} \right) \cdot \vec{n} \, dS = \int_{cs} \left(\vec{U}^* \cdot \vec{n} \right) dS. \tag{14}$$

Once the pressure is obtained, the intermediate velocity can be corrected and updated to obtain the final velocity by:

$$\vec{u}^{n+1} = \vec{u}^* - \Delta t \left(\vec{\nabla} p^{n+1} \right)_{cell\ center} \quad \text{and} \quad \vec{U}^{n+1} = \vec{U}^* - \Delta t \left(\vec{\nabla} p^{n+1} \right)_{cell\ face}. \tag{15}$$

3.2. Lagrangian moving interface and fixed Eulerian grid

Within the fixed-grid framework, the sharp interface is identified and tracked by separate marker points to form the Lagrangian portion of this method. The interface can be either fixed solid boundaries (pipe wall) or moving phase boundaries (liquid–gas interface). With moving phase boundaries, the motion of the interface is tracked through the translation of the marker points over the stationary, Cartesian grid. These marker points that are connected by quadratic curve fitting are employed to capture the deformation and movement of the sharp interface. The overall solution is obtained by matching the mass and momentum fluxes from both phases at the sharp interface.

The computational framework is built on an Eulerian Cartesian grid to facilitate the field equation computation. For each phase domain, a second-order accurate two-step fractional step method within the finite-volume framework [22,25] is used to numerically integrate the governing equations in that phase. Also, a cell-centered, collocated (non-staggered) approach is adopted.

3.3. Sharp interface method with cut-cell technique (SIMCC)

The sharp interface method with cut-cells (SIMCC) has four main algorithmic procedures: interfacial tracking, the merging procedure, the flux computations in the interfacial region and the moving interface algorithm for advancing the interface. The first three are needed for a stationary object embedded in the underlying Cartesian grid. Moving interface algorithm is used for advancing the interface for moving or deforming objects and is discussed in the next section.

The cut-cell approach developed in [18] is used to handle irregular intersections between an interface and the Cartesian grid. Because of the interface, some cells are cut and can not maintain their rectangular shape anymore require special treatment. These cells are called 'cut-cells'. Fig. 4 illustrates the formation of cut-cells where the regular grid is cut by the interface.

For interfacial tracking, information about the interface needs to be stored in a way which allows for easy computations. In the present research, positions of marker points are fitted by piecewise-quadratic curves. From these curves, various geometrical quantities like the normal, curvature and the intersections between the interface and background grid can be easily calculated. The distance between the marker points is adjusted at every time step to get a more or less uniform distribution on the interface. Information about the intersections is needed to know which cells have been cut by the interface and need to be reconfigured. This information is also used for the next step, the merging procedure.

Using the merging procedure, the fragments of cells intersected by the interface can be merged with neighboring cells or with larger fragments to form the cut-cells. For the purpose of forming cut-cells, the interface is assumed to be formed by a sequence of
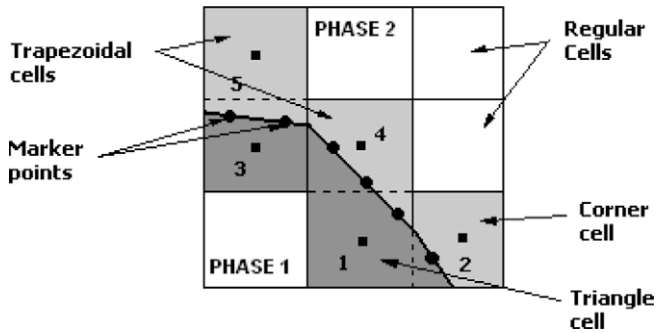
Fig. 4. An example of cut-cells formed near the interface.

straight line sections. The possible shapes of cut-cells that can be formed after the merging procedure are trapezoidal, triangular and pentagonal (or corner cells). The new grid is formed by the regular cells and the special cut-cells. Fig. 4 illustrates the formation of interfacial cells where cells 1–4 are cut by an interface. According to the present cut-cell technique, the segments of an interfacial cell not containing the original cell center are absorbed by their neighboring cells; the segments containing the original cell center are given the same index as the original cell. For example, in Fig. 4, the upper segment of cell 3 is absorbed into cell 5 to form a new trapezoid cell. The fraction of cell 3 with cell center becomes a new independent trapezoid cell. The main segment of cell 1 that contains the original cell center will absorb the small segments of cells 4 and 2 to form a new triangular cell. The remaining segment of cell 2 containing its original cell center now becomes an independent pentagonal cell. With these cut-and-absorption procedures, the interfacial cells are reorganized along with their neighboring cells to form new cells with triangular, trapezoidal, and pentagonal shapes in a 2d domain. After this procedure, each newly defined cell maintains a unique index and cell center to support the needed data structure. Most cells still keep their original shapes. Also, the number of cells does not change in this operation.

It is important to know the shape of the newly formed cut-cells for the third technique, which is flux computations. It is also important to know on which side of the cut-cell the interface lies. A special interpolation scheme with a higher order accuracy is required to handle the complicated cut-cells to get the accurate primary variables or derivatives at the center of a cell face. The interpolation is one-sided in the sense that only the variable values for one phase are used to evaluate the derivatives etc. for that phase. For more details, refer to [6,20,21].

The original Cartesian grid will now become a mixed grid which includes some of the original structured grid and the unstructured grid due to the newly generated cut-cells. Fig. 1 is an example of the mixed structured and unstructured type grid obtained after the merging procedure.

Since the number of cells in SIMCC is not changed during the reorganization of the grid, the matrix of coefficients of SIMCC is very similar to the original one for the cylindrical coordinate system. SIMCC can be used to solve fluid flow and heat transfer problems involving more than one phases and/or a complex geometry with a high accuracy. However, due to the cut-cell algorithms and data management requirements, SIMCC is computationally intensive. In SIMCC, only a small percentage of coefficients (those corresponding to the cut-cells) have to be modified so that the convergence behavior and characteristics is very close to the curvilinear system. Therefore it converges much faster than unstructured grid solvers. Consistent interpolation formulas are chosen for estimation of the fluxes along any of the cell surfaces. Both inviscid and viscous terms can be handled to maintain a globally second-order accurate algorithm.

3.4. Moving interface algorithm

The techniques discussed up to this point constitute all the elements required to obtain the solution for a stationary interface. However, for most problems in multiphase flows, the interface is not fixed and therefore a moving interface algorithm is necessary. The moving interface algorithm in this research includes two functions. The first one is to advance the interface, which is based on ideas of [20,26] and the second one is to update the cells because of change of phase [27].

In the unsteady multiphase computation, the interface will advance to satisfy the interfacial dynamics in each time step. In SIMCC, a 'push and pull' strategy is used to determine the new location of an interface and also to satisfy the force balance at the interface. The forces acting at the interface can be divided into the normal and tangential components. The displacement of interface is governed basically by the normal forces at the interface, while the tangential forces cause the circulation inside and outside the bubble.

In this 'push and pull' strategy, only the normal component of force balance is considered on the interface and the new location of interface will be determined by a series of iterations. The local imbalance Π between the total normal stress which includes both static and dynamic pressure and viscous contributions and surface tension forces is defined as:

$$\Pi(s) \equiv \frac{2}{Re}\left[\left(\frac{\partial u_n}{\partial n}\right)_l - \left(\frac{\mu_v}{\mu_l}\right)\left(\frac{\partial u_n}{\partial n}\right)_v\right] - P_l + P_v - \frac{\kappa}{We}, \qquad (16)$$

where P_l and P_v are the total pressures in the liquid and vapor, respectively. For example, in $k + 1$ iteration, the residual of the force balance in the normal direction will be computed and the displacement of marker points is assumed proportional to this residual:

$$\begin{aligned} X_{int}^{N+1,k+1} &= X_{int}^{N+1,k} + \beta \cdot \Pi^k(s) \cdot n_x, \\ Y_{int}^{N+1,k+1} &= Y_{int}^{N+1,k} + \beta \cdot \Pi^k(s) \cdot n_y, \end{aligned} \qquad (17)$$

where (X_{int}, Y_{int}) are the coordinates of marker points, (n_x, n_y) are the components of normal vector in the x- and y-direction, respectively. β is an empirical relaxation factor and it has a value normally in the range of 0.01–0.0001 in this research.

Fig. 5 is an illustration for this interfacial advancing process. In Fig. 5, a marker point A_0 is located at the initial interface and the residual of force balance in the normal direction Π_1 will be computed. Based on the location of A_0 and the value of Π_1, the marker point will be pushed to A_1. In this moment, the residual of force balance in the normal direction will be checked. If the new residual Π_2 is still large, the marker point A_1 will be pushed to A_2. Once the residual is small enough which means that the force balance in the normal direction has achieved convergence, the iteration will be stopped and the normal component of interfacial velocity for time step $N + 1$ can be determined by:
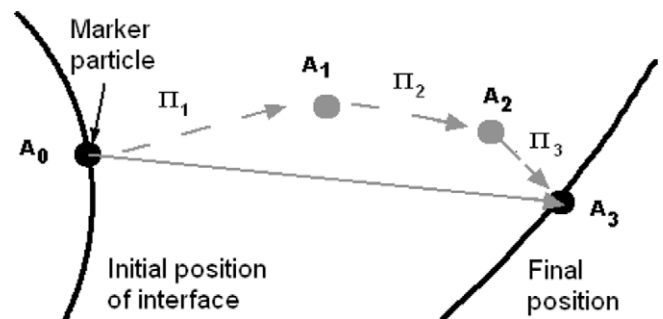

Fig. 5. Illustration of interfacial advancing process.

$$u_{int,n}^{N+1} = (X_{int}^{N+1} - X_{int}^N)/\Delta t,$$
$$v_{int,n}^{N+1} = (Y_{int}^{N+1} - Y_{int}^N)/\Delta t. \qquad (18)$$

In this iterative procedure, the residual of the force balance in the normal direction is required to be less than 1.0E−3. Additionally, in cases where the interface completely encloses one phase, as in the present study, the local increment in the location of interface markers should be done in such a way as to satisfy mass conservation for the enclosed phase. For constant density, this translates to conserving the volume of the enclosed phase. It has been shown in [20,26] that mass conservation is satisfied if the following condition on Π is satisfied:

$$\int_0^s \Pi^k(s)\,ds = 0. \qquad (19)$$

This mass constraint also determines a free constant of the pressure field in the total normal stress at each iteration k. Even after this constraint has been satisfied, there may be a small change in the bubble volume due to higher order numerical errors. To prevent these errors from accumulating, a simple scaling of the interface is done at each time step. The uniform scaling magnitude Δ of the interface in the normal direction can be determined from

$$\Delta \int_0^s 2\pi y_{int}\,ds = \Delta V, \qquad (20)$$

where ΔV is the error in the volume, and the integral evaluates the surface area. This simple scaling technique is very effective in maintaining the mass conservation. The percentage error can be controlled to within 10^{-5} in two or three iterations.

The tangential stress balance equation is used to find the tangential velocity at the interface in a similar way, by defining a local imbalance Σ:

$$\Sigma(s) \equiv \left(\frac{\partial u_s}{\partial n} + \frac{\partial u_n}{\partial s}\right)_l - \left(\frac{\mu_v}{\mu_l}\right)\left(\frac{\partial u_s}{\partial n} + \frac{\partial u_n}{\partial s}\right)_v. \qquad (21)$$

A similar iterative procedure is employed to find the tangential velocity component. A velocity proportional to the stress imbalance Σ is imparted locally to the marker points:

$$u_{int,s}^{N+1,k+1} = u_{int,s}^{N+1,k} + \gamma \cdot \Sigma^k(s) \cdot n_y,$$
$$v_{int,s}^{N+1,k+1} = v_{int,s}^{N+1,k} - \gamma \cdot \Sigma^k(s) \cdot n_x, \qquad (22)$$

where γ is determined empirically. Thus, the normal and tangential velocity components for the interface are determined using the interfacial stress balance conditions. In the absence of mass transfer, the velocities of the two phases are continuous at the interface.

4. Verification and validation

Axisymmetric, laminar, steady flow over a sphere is studied. This problem tests the cut-cell algorithm employed for solving flow over an arbitrary smooth surface. This test case is very similar to the case of flow over a vapor bubble and can test the accuracy of SIMCC. Various parameters like wake length, vortex center, and coefficient of drag were calculated and compared with numerical
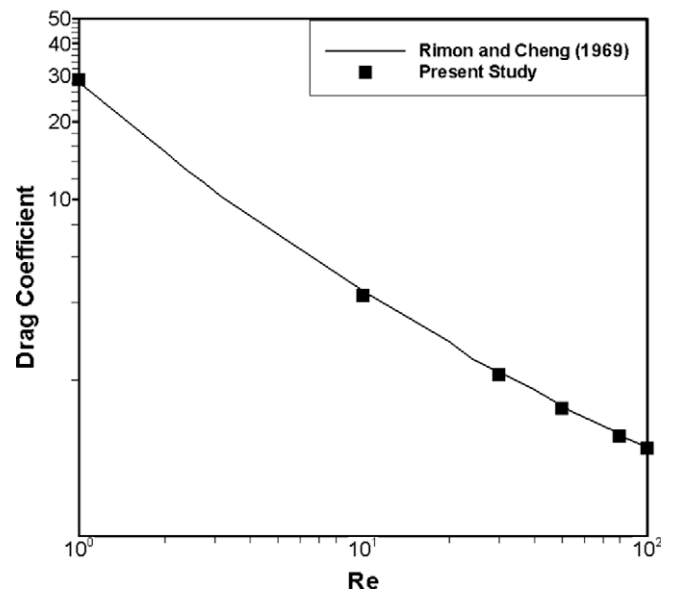
Fig. 7. Drag coefficient of solid sphere.
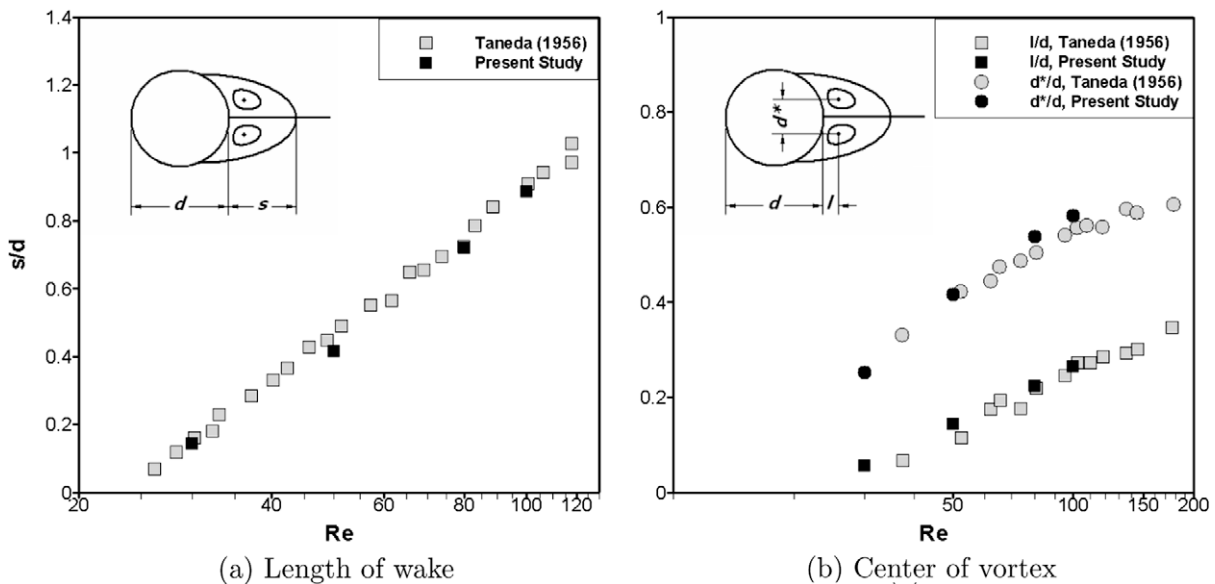
(a) Length of wake

(b) Center of vortex

Fig. 6. Wake behind solid sphere.

and experimental results for Reynolds number in the range 1–100. Above Reynolds number of about 130, the flow becomes unsteady and vortex shedding occurs [28]. Hence, we have restricted ourselves to this range of Reynolds number.

The computational domain was chosen to be 15d in length and 5d in width, where d is the sphere diameter. On the left boundary, a unit inlet velocity is prescribed. The lower boundary is symmetric due to the assumption of axisymmetry. The far-field boundary condition must be used for the top and right boundary for accurate results. A uniform grid resolution of 0.05 has been used. This corresponds to 20 cells spanning the width of the sphere. The grid spacing was chosen on the basis of a grid refinement study.

Simulation was done for Re in the range of 1–100. It was found that flow separation occurs at $Re = 25$. This is in agreement with [28] who found an experimental value of $Re = 24$ at which separation occurred. For $Re = 30$ and higher, wake length and the vortex center have been compared with the experimental results of [28]. Fig. 6(a) and (b) shows good agreement both in terms of the trend and the actual calculated values. In Fig. 7, the calculated coefficient of drag is compared with the numerical results of [29]. The

error is found to be within 3% for all the six cases. This proves that the present code can calculate the drag over a surface very accurately using SIMCC.

5. Numerical results and discussion

5.1. Bubble shape

Simulation was done for Re in the range of 1–100, and We in the range 1–10. The computed shapes have been shown in Fig. 8. We see that the shapes are in good agreement with those calculated by other researchers [2,30]. Results for $Re = 0.5$, $We = 0.5$, and $Re = 1.0$, $We = 1.0$ are given in Fig. 9, and compared to the shapes calculated for the same parameters using the asymptotic formula of [1]. The solution by [1] has been derived under the assumptions that $Re \ll 1$, $We \ll 1$, and $Re^2 \ll We$. It can be seen that the agreement between our solution and that given by the asymptotic theory of [1] is very good.

5.2. Shape transition

Fig. 10 shows the streamlines near the bubble after it has reached steady state. The shape of the bubbles changes from spherical to oblate spheroid with an increase in We. For $Re = 1$, the bubble begins to flatten at the rear end with increasing We, and finally has a sort of indentation at $We = 10$. This can be seen clearly in Fig. 10(a). Also, the shape of the bubble does not seem to change much on increasing the We.

Looking at Fig. 8, it can be noted that there is a change in the shape of the bubbles between $Re = 10$ and $Re = 100$, for the whole range of We studied. At $Re = 100$, the bubbles begin to have greater deformation at the front end. This becomes more and more obvious as We increases. At $We = 10$ we actually have an indentation at the front end of the bubble. To understand this transition, we simulated a case with $Re = 50$, $We = 3$. The results are shown in Fig. 10(c). It is seen that the shape of the bubble is nearly symmetrical. This finding is consistent with the results reported by [2] who also found that this kind of shape transition occurs for $Re = 100$. They too report that $Re = 50$ is the border line case and seems to have fore-aft symmetry.
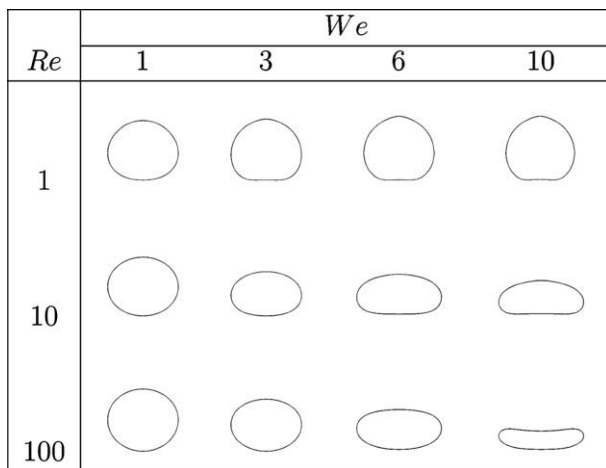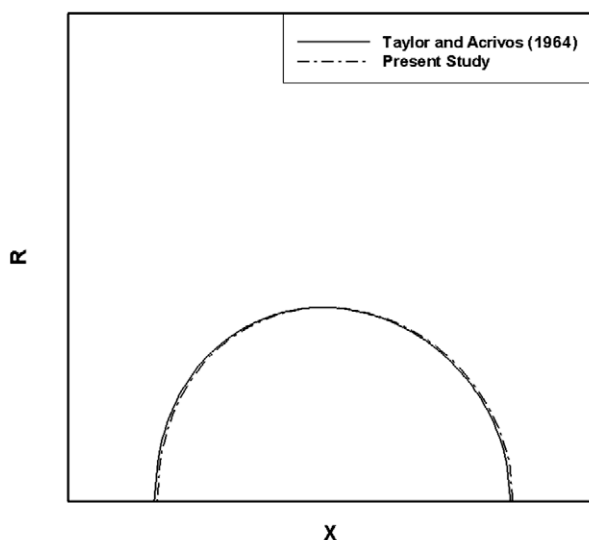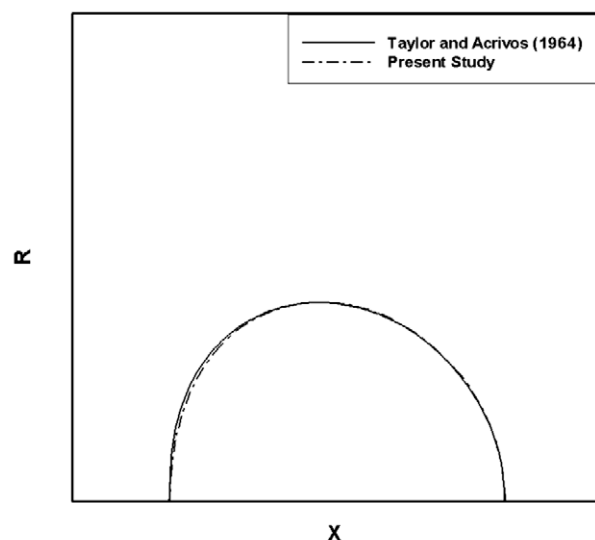
Fig. 8. Computed bubble shapes.

(a) Re=0.5, We=0.5

(b) Re=1, We=1

Fig. 9. Comparison of bubble shape with [1].

To characterize this transition further, we looked at the surface tension on the bubbles for *We* = 3, at the four different *Re* in Fig. 11. The shape of the bubble directly depends on the net surface tension force acting on it. Surface tension is given by the curvature divided by *We*, and since the latter is the same for all the four cases, we can compare the curvature of the bubbles. It is seen that for *Re* = 50, the curvature is nearly the same at the front and rear. This implies that for this case, the normal forces on the front and the rear of the bubble are such that their cumulative effect produces the approximately same surface tension force on the bubble. Also, the highest curvature occurs almost exactly at the center of the bubble, indicating the flattening effect at both the front and rear surfaces. For *Re* = 1, the curvature is highly asymmetrical, indicating that the shape of the bubble too lacks fore-aft symmetry. The

curvature is negative at the rear end, because of the indentation. Thus, we see that the curvature and therefore the shape of the bubble are a strong function of the Reynolds number.

5.3. Bubble shape aspect ratio

In Fig. 12 the aspect ratio of the bubbles is compared to [30] for *Re* = 10 and 100. The comparison is very favorable. It is seen that the aspect ratio is a very strong function of the Weber number. High *We* implies weaker surface tension which gives higher deformation, while the limit *We* = 0 corresponds to infinite surface tension and perfectly spherical bubble. The aspect ratio is also influenced by *Re*, higher *Re* giving higher deformation as well.
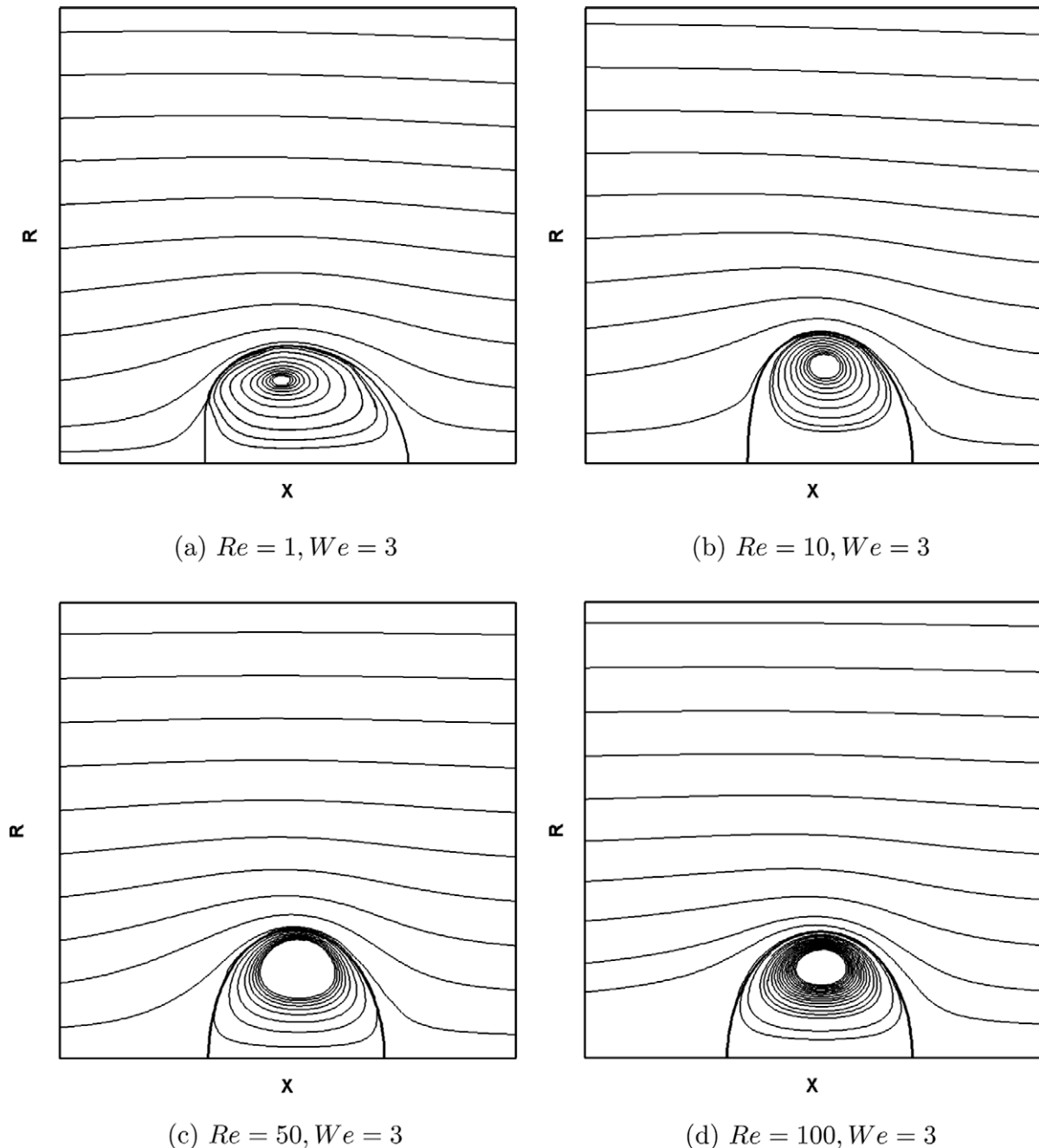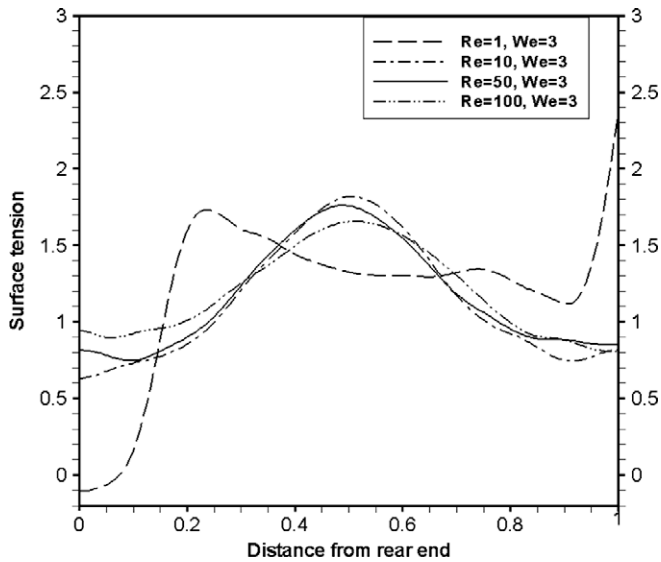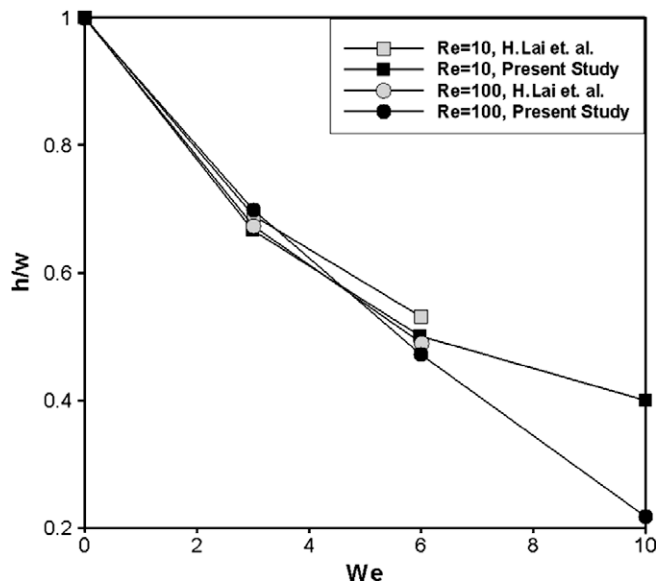

(a) $Re = 1, We = 3$

(b) $Re = 10, We = 3$

(c) $Re = 50, We = 3$

(d) $Re = 100, We = 3$

Fig. 10. Transition in shape.

Fig. 11. Influence of *Re* on the curvature of bubble.

Fig. 12. Influence of *We* on aspect ratio.

5.4. Circulation

A region of circulation develops behind the bubble for higher *We*. Fig. 13 shows the wake behind the bubble for different *Re*. The circulation is just evident at *Re* = 1, while by *Re* = 100 there is a fully formed detached circulation zone behind the bubble.

5.5. Time-dependent drag

We also present results for the drag on the bubbles. The drag force on the bubble derives from three types of forces: dynamic pressure, normal stress and shear stress. By integrating these forces on the surface of the bubble, we arrive at the pressure drag, normal drag and shear drag respectively. The coefficient of drag is defined as follows:

$$C_D = \frac{8F_D}{\rho_l U^2 \pi d^2},\tag{23}$$

where F_D is the force, d is the equivalent diameter of the bubble, and U is the terminal velocity. The contributions from these three components have been shown in Figs. 14 and 15 for two representative cases. The figures show how the forces on the bubble develop during the unsteady simulation. When the drag on the bubble becomes relatively constant it means that the bubble has reached its terminal velocity and shape. In these computations, the initial drag force on the bubble is not zero. This is because the bubble is initially stationary in a gravitational force field. Therefore in numerical simulations, the 'push and pull' strategy attempts to balance this gravitational force on the bubble by the pressure forc

In the figures, the total drag coefficient matches well with other published results. For *Re* = 10, *We* = 3 we obtain C_D = 3.4, which compares well with the value of 3.3 calculated by [2]. For *Re* = 100, *We* = 3, [2] predict a value of C_D = 0.62. In our simulations, we obtain a value of 0.61.

From Figs. 14 and 15, several observations about the unsteady dynamics can be made. First of all, we note that the normal drag and the pressure drag seem to be complementary to each other. At the start of the simulation, since the bubble is stationary, the normal and shear stress on the bubble are negligible. During the simulation, as the bubble accelerates and deforms the contribution of the pressure forces to the total drag decreases, while the normal and shear forces increase in magnitude.

Another feature of the flows is that the contribution of the shear drag to the total drag decreases with increasing Reynolds number. At *Re* = 10, we find that shear drag is responsible for almost ten
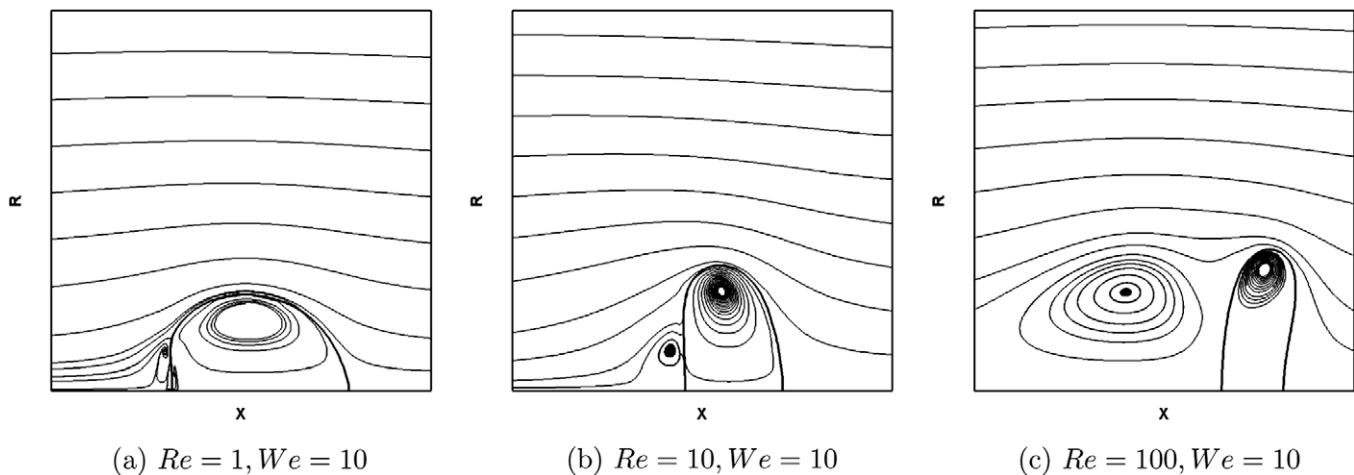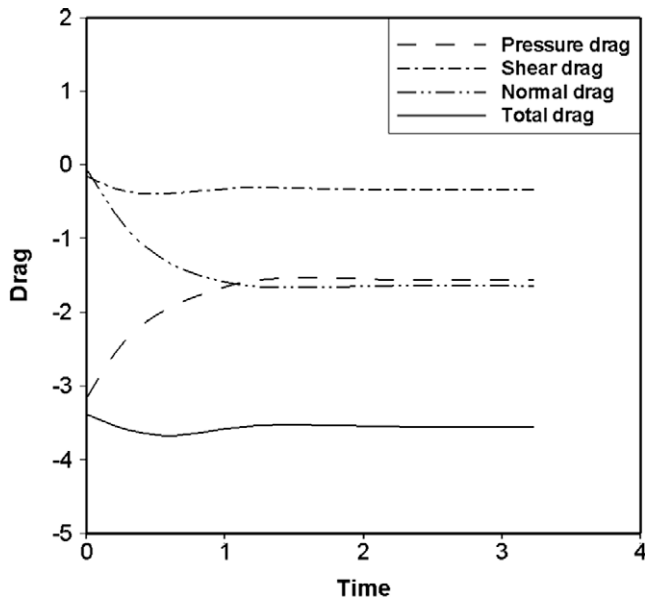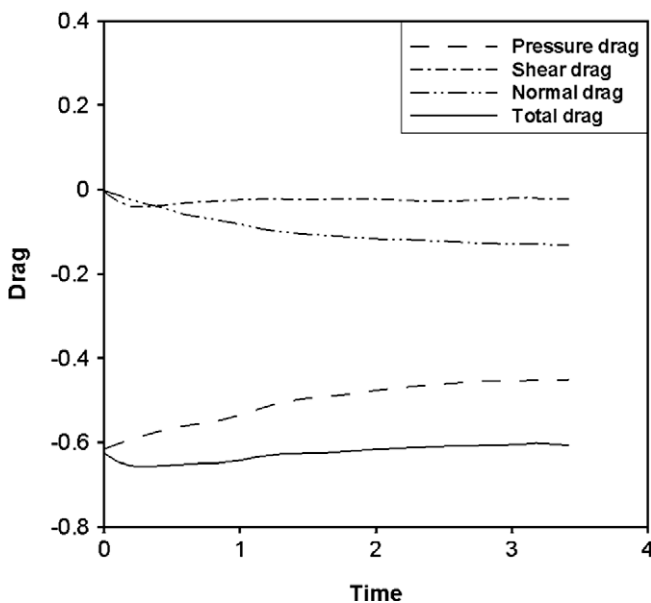

(a) $Re = 1, We = 10$ (b) $Re = 10, We = 10$ (c) $Re = 100, We = 10$

Fig. 13. Development of circulation region.

Fig. 14. Drag history, $Re = 10$, $We = 3$.

Fig. 15. Drag history, $Re = 100$, $We = 3$.

Table 1
Drag on deformable bubble, compared to *[30] and **[26].

$Re\backslash We$	1	3	6	10
1	27.34	28.30	23.80	21.22
	19.22*	20.57*	19.10**	–
10	3.01	3.40	3.23	2.78
	2.64*	3.23*	3.67**	4.16**
100	0.45	0.61	1.28	2.15
	0.42*	0.62**	1.23**	2.77**

the present interfacial advection technique, that can satisfy the stress balance at the interface in an approximate manner. This is a problem only for very low Re ($Re \leqslant O(1)$) flows in which the viscous stresses are substantial. Also, since the error in the computations is of second order, it is mainly the drag force which is affected. The shape calculations are not affected by these second-order errors.

6. Conclusion

The numerical method called SIMCC with moving interface algorithm has been described for calculating multiphase flows. Then the SIMCC method was validated by using flow over solid sphere. The method was able to accurately predict the drag on the sphere in the range $1 < Re < 100$. Next, the moving interface algorithm was validated by computing flows around moving, deformable bubbles. Results were presented in the form of streamline plots, aspect ratio and drag. It has been shown that the present method is fully capable of dealing with free interfaces that can move or deform. SIMCC is able to calculate the drag on deformable interfaces, and presents an alternative to methods that use body-fitted adaptive grids [3,26,30].

An important contribution of the present research is that the components of the drag force on bubble have been calculated separately and analyzed. It was found that at lower Re, the shear stress and the normal stress have a significant contribution to the total drag on bubble. Therefore, it would be erroneous to neglect the shear stress on the bubble and treat it as a 'free' surface. At higher Re, the shear stress contribution to the drag becomes negligible.

In summary, the new contribution of the current manuscript is on the unsteady hydrodynamics of a bubble. As far as we know, this paper is the first to present time-dependent drag of a deformable bubble.

percent of the total drag. At $Re = 100$, this contribution drops to about four percent. This finding is consistent with the physics of the problem, since the viscous stresses are lower at higher Re. We also note that the contribution of the normal viscous stresses is significantly reduced with increasing Re. At $Re = 10$, pressure and normal drags seem to have an almost equal contribution to the total drag on the bubble, but at $Re = 100$, the normal drag is only about 20% of the total drag. In fact, at $Re = 100$, pressure drag dominates, and this trend is similar to what is observed with flow over rigid spheres.

In Table 1, we show the results for the total drag on the bubble. The range for Reynolds numbers investigated is $1 < Re < 100$, and that of Weber number is $1 < We < 10$. The first line for each case shows results from SIMCC. The second line shows results by [26,30]. It is seen that the results are in good agreement with those by [26,30], except for the case where $Re = 1$. This is a limitation of

References

[1] T.D. Taylor, A. Acrivos, On the deformation and drag of a falling viscous drop at low Reynolds number, J. Fluid Mech. 18 (1964) 466–476, doi:10.1017/S0022112064000349.
[2] G. Ryskin, L.G. Leal, Numerical solution of free-boundary problems in fluid mechanics. Part 2. Buoyancy-driven motion of a gas bubble through a quiescent liquid, J. Fluid Mech. 148 (1984) 19–35.
[3] D.S. Dandy, L.G. Leal, Buoyancy-driven motion of a deformable drop through a quiescent liquid at intermediate Reynolds numbers, J. Fluid Mech. 208 (1989) 161–192, doi:10.1017/S0022112089002818.
[4] F. Raymond, J.M. Rosant, A numerical and experimental study of the terminal velocity and shape of bubbles in viscous liquids, Chem. Engrg. Sci. 55 (2000) 943–955.
[5] H. Lai, H. Zhang, Y. Yan, Numerical study of heat and mass transfer in rising inert bubbles using a conjugate flow model, Numer. Heat Transfer Part A: Appl. 46 (2004) 79–98.
[6] H.S. Udaykumar, R. Mittal, P. Rampuggoon, A. Khanna, A sharp interface Cartesian grid method for simulating flows with complex moving boundaries, J. Comput. Phys. 174 (2001) 345–380.
[7] T. Ye, W. Shyy, C. Tai, J. Chung, Assessment of sharp-and continuous-interface methods for drop in static equilibrium, Comput. Fluid 33 (2004) 917–926.
[8] C.S. Peskin, Numerical analysis of blood flow in the heart, J. Comput. Phys. 25 (1977) 220–252.

[9] M. Francois, Computations of Drop Dynamics with Heat Transfer, Ph.D. Thesis, University of Florida, 2002.

[10] C.W. Hirt, B.D. Nichols, Volume of fluid (VOF) method for thermodynamics of free boundaries, J. Comput. Phys. 39 (1981) 201–225.

[11] J.E. Pilliod, E.G. Puckett, Second-order accurate volume-of-fluid algorithms for tracking material interfaces, J. Comput. Phys. 199 (2004) 465–502.

[12] M. Ni, M. Abdou, S. Komori, A variable-density projection method for interfacial flows, Numer. Heat Transfer Part B 44 (2003) 553–574.

[13] S. Tanguy, A. Berlemont, Application of a level set method for simulation of droplet collisions, Int. J. Multiphase Flow 31 (2005) 1015–1035.

[14] G. Son, Efficient implementation of a coupled level-set and volume-of-fluid method for three-dimensional incompressible two-phase flows, Numer. Heat Transfer Part B 43 (2003) 549–565.

[15] M. Sussman, A second order coupled level set and volume-of-fluid method for computing growth and collapse of vapor bubbles, J. Comput. Phys. 187 (2003) 110–136.

[16] G. Caginalp, Applications of Field Theory to Statistical Mechanics, Springer-Verlag, Berlin, 1984.

[17] W. Shyy, H.S. Udaykumar, M.M. Rao, R.W. Smith, Computational Fluid Dynamics with Moving Boundaries, Taylor and Francis, Washington, DC, 1996.

[18] T. Ye, W. Shyy, J.N. Chung, A fixed-grid, sharp-interface method for bubble dynamics and phase change, J. Comput. Phys. 174 (2001) 781–815.

[19] C. Tai, W. Shyy, Multigrid computations and conservation law treatment of a sharp interface method, Numer. Heat Transfer Part B 48 (2005) 405–424.

[20] T. Ye, Direct Numerical Simulation of a Translating Vapor Bubble with Phase Change, Ph.D. Thesis, University of Florida, 2001.

[21] C.F. Tai, Cryogenic Two-phase Flow and Phase-change Heat Transfer in Microgravity, Ph.D. Thesis, University of Florida, 2008.

[22] J.H. Ferziger, M. Peric, Computational Methods for Fluid Dynamics, Springer-Verlag, 1996.

[23] J. Chorin, Numerical solution of the Navier–Stokes equations, Math. Comput. 22 (1968) 745–762.

[24] J. Kim, P. Moin, Application of a fractional step method to incompressible Navier–Stokes equations, J. Comput. Phys. 59 (1985) 308–323.

[25] Y. Zang, R.L. Street, J.R. Koseff, A non-staggered grid, fractional step method for time-dependent incompressible Navier–stokes equations in curvilinear coordinates, J. Comput. Phys. 114 (1994) 18–33.

[26] G. Ryskin, L.G. Leal, Numerical solution of free-boundary problems in fluid mechanics. Part 1. The finite-difference technique, J. Fluid Mech. 148 (1984) 1–17.

[27] H.S. Udaykumar, H.C. Kan, W. Shyy, R. Tran-Son-Tay, Multiphase dynamics in arbitrary geometries on fixed Cartesian grids, J. Comput. Phys. 137 (2) (1997) 366–405.

[28] S. Taneda, Experimental investigation of the wake behind a sphere at low Reynolds numbers, J. Phys. Soc. Jpn. 11 (10) (1956) 1104–1108.

[29] Y. Rimon, S.I. Cheng, Numerical solution of a uniform flow over a sphere at intermediate Reynolds numbers, Phys. Fluids 12 (5) (1969) 949–959.

[30] H. Lai, Y.Y. Yan, C.R. Gentle, Calculation procedure for conjugate viscous flows about and inside single bubbles, Numer. Heat Transfer Part B 43 (2003) 241–265.